Global Brain Flexibility During Working Memory Is Reduced in a High Genetic Risk Group for Schizophrenia

Supplementary Information

Contents

Full Description of Methods

Sample: Participant stratification by SCZ-PRS

Participant recruitment was based on the stratification of the ALSPAC birth cohort by polygenic risk for schizophrenia. During the 2 ½ years of scanning procedure, we attempted to balance the gender between the two groups and to get both low and extreme high groups for polygenic risk score sampled from a large cohort available from the BRISTOL ALSPAC team (N=8169).

Pregnant women resident in Avon, UK with expected dates of delivery 1st April 1991 to 31st December 1992 were invited to take part in the study. The initial number of pregnancies enrolled is 14,541. Of these initial pregnancies, there was a total of 14,676 foetuses, resulting in 14,062 live births and 13,988 children who were alive at 1 year of age.

When the oldest children were approximately 7 years of age, an attempt was made to bolster the initial sample with eligible cases who had failed to join the study originally. Please note that the study website contains details of all the data that is available through a fully searchable data dictionary and variable search tool" and reference the following webpage: http://www.bristol.ac.uk/alspac/researchers/our-data/

Approximately, 11000 children have provided samples and have DNA available. Of these, 8365 individuals were genotyped on Illumina 550 platform and 8169 of them had passed the significant threshold (p-value) derived from genome-wide association studies (GWAS) and passed the quality control. The two groups were well-balanced according to their gender ratio and age distribution (see below). No subject was receiving psychotropic medication. Ethical approval for the study was obtained from the ALSPAC Ethics and Law Committee and the Local Research Ethics Committees.

We assessed 197 individuals - 99 individuals (52 female, 47 male) with low SCZ-PRS and 98 individuals (52 female, 46 male) with high SCZ-PRS from either tail of the SCZ-PRS distribution from a large, genotyped population of similar age (see S1). We started recruitment at the lowest and highest extremes of the SCZ-PRS distribution aiming to recruit two groups of high and low PRS subjects each with 100 members with the same gender balance. By design, there were highly significant differences between the SCZ-PRS for the two groups ($P < 5 \times 10^{-15}$). The ALSPAC team sent out 1241 invitations in total (470 to the low and 771 to the high SCH-PRS group).

The SCZ-PRS was calculated using summary statistics from PGC-SCZ2 (1) at a threshold of $P \leq .05$, approximately 5% of all imputed SNPs. This threshold was specifically chosen as it captures the most

SCZ liability (most variance explained) in the primary PRS analysis using training data/summary statistics derived from the largest SCZ GWAS of 34241 SCZ cases and 45604 controls.

Both SCZ-PRS groups are more than 1 SD above / below the population mean. z-transformed PRS by group is showed in S1 [1]. The mean group z-PRS is above 1.5 (1.42 for high, 1.71 for low ; see Table S1).

Table S1. Mean group z-PRS estimated over the whole population of 8169 individuals showed in S1.

Group	N	Z-PRS	Z- PRS SD
High	98	1.42	0.58
Low	99	-1.71	0.46
Non-Imaging	8168	0.00	0.98

The study was approved by the Central Bristol Research Ethics Committee (13/SW/0170). We assessed 197 individuals - 99 (52 female, 47 male) individuals with low SCZ-PRS and 98 individuals (52 female, 46 male) with high SCZ-PRS from either tail of the SCZ-PRS distribution from a large, age-matched, genotyped population (Figure 1). There were highly significant differences between the SCZ-PRS for the two groups ($P < 5 \times 10^{-15}$). There was however evidence of violation of homoscedasticity between the SCZ-PRS groups), where the cluster was more diffuse for the high SCZ-PRS compared to the low SCZ-PRS group (Levene's test: $F_{1,195} = 16.1$, $P = 0.00083$; Fligner-Killeeen; $P < .001$). For further details about this cohort and the multimodal imaging protocol, see [1].

Psychotic experiences and WISC-III measures are tabulated in Table S2 in conjunction with the statistical analysis. For further details, see [1]. We observed a nominal association between psychotic experiences and high SCH-PRS untangling an increased pattern and no nominal association between WISC measures with SCH-PRS.

Table S2. OR and β Coefficients (±95% Confidence Intervals) for Psychotic Experiences and WISC-III IQ Measures by SCZ-PRS Group (Higher OR/Coefficients Reflect an Association With the High SCZ-PRS Group)

Phenotype	Estimate	Lower 0.95%	Upper 0.95%	*P*
Psychotic experiences	1.100[a]	1.00660	1.20283	.039
WISC-III (verbal)	0.217[b]	−4.48233	4.91643	.927
WISC-III (performance)	1.944[b]	−2.83438	6.72296	.423
WISC-III (total)	1.606[b]	−2.77053	5.98341	.470

[a]Odds ratio (OR).
[b]β coefficients.

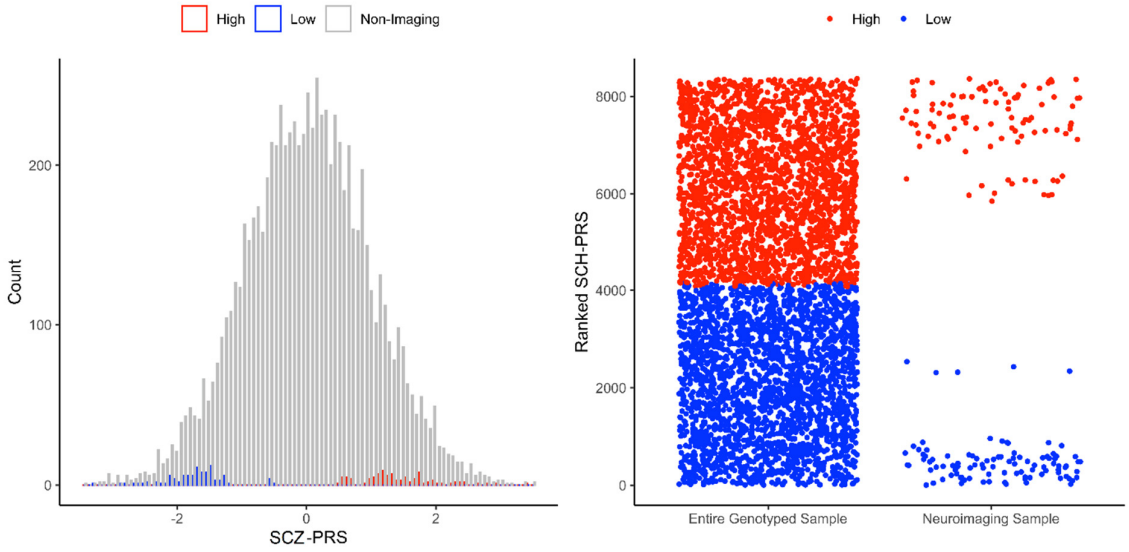

Figure S1. Characterisation of the schizophrenia polygenic risk group in the neuroimaging sample (calculated by SCZ-PRS - left; defined by rank – right; N=197; Low = 99, High = 98) compared to the entire genotyped cohort (N=8169, not including the neuroimaging sample).

Experimental Setup and Procedure

Participants were placed in a supine position in the MRI scanner. Padding was placed under the knees in order to maximize comfort and provide an angled surface to position the stimulus response box. Finally, in order to minimize head motion, padded wedges were inserted between the participant and head coil of the MRI scanner. For all sessions, participants performed a cued sequence production (CSP) task (see Figure S1), responding to visually cued sequences by generating responses using their right-hand on a fiber-optic response box. Responses were made using four fingers of the left hand (the thumb was excluded). Visual cues were presented as a series of Arabic numbers from 1 to 4. Each number was mapped to one of the four buttons on the response box. We designed an n-back experiments with three load levels (0, 1 and 2) following the same order during the 6 runs. The total number of presented numbers for each n-back level per run was 10 which means 10 responses for 0-back level, 9 response for 1-back level and 8 response for the 2-back level. The sequence of presented numbers was generated via a randomization procedure for each participant. Every block started with a label {‘0-back’ ,’1-back’,’2-back’} to notify the participant of the current n-back level. At the end of the experiment, we showed a message {‘END – PLEASE DON’T MOVE’}.

During the task, participants were not informed about their performance. **S2** illustrates an example of an n-back task setup.

Each number (trial) was presented for 2 seconds, separated by an inter-trial interval (ITI) lasting maximum 3s, not including any time remaining from the previous trial. The duration of each block/run was fixed. Responses and reaction times to each stimulus were for subsequent analysis of behavioural performance. Participants completed 6 runs of each of three conditions. The total duration of the experiment was ~ 10 minutes with 9 minutes the actual block/run time. Each block/run includes 15 slices with a total duration of 30 sec.

Participants had performed the same task earlier on the same day as part of a MEG acquisition, and so were already familiar and practiced with the task when peforming during the MRI acquisition. Stimulus presentation was performed by MATLAB version 7.6 (Mathworks, Natick, MA) using the Psychophysics Toolbox version 3. Key-press responses were collected using a fiber-optic button box supplied by NATA Technologies (Coquitlam, BC).

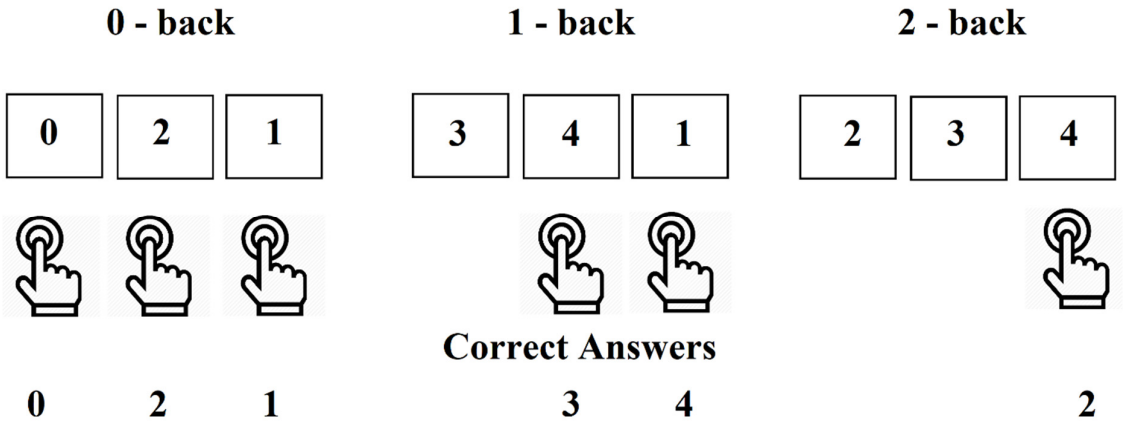

Figure S2. n-back paradigm (example: for zero, one and two-back target).
Upper row demonstrates the working memory test for each n-back level , middle row represents the response of the participant while the last row demonstrates the correct answer per n-back block.

Acquisition and Preprocessing of fMRI Data

MRI data were obtained on a GE HDx 3 Tesla scanner. Whole brain, dual-echo, BOLD GE-echoplanar imaging (EPI) images (repetition time (TR) = 2 s, echo time (TE1) = 13 ms, TE2 = 31 ms, voxel-size 3.5 × 3.5 × 3 mm^3, 293 slices in total) were collected.

Gradient echoplanar imaging data was acquired for each subject on the same 3T GT HDx system with an eight channel receiver at CUBRIC (Cardiff University Brain Research Imaging Centre), School of Psychology, Cardiff University (parameters: 35 slices, slice thickness; 3mm/1mm gap, acquisition matrix; 64 x 64; FOV; 220mm, TR 2000ms, TE 35ms, flip angle 90°, acceleration (ASSET) factor; 2, 256 volumes – approximately 9 minutes). All functional images were first motion scrubbed, where TRs with a frame wise displacement > 0.9 were removed, as previously recommended [1]. Image processing and statistical analyses were conducted using statistical parametric mapping methods as implemented in FMRI Expert Analysis Tool (FEAT, Version 5.98, part of FMRIB's Software Library, www.fmrib.ox.ac.uk/fsl [2]). The following pre-statistics processing was applied; motion correction using MCFLIRT ; slice-timing correction using Fourier-space time-series phase-shifting; non-brain removal using BET (Brain Extraction Tool) spatial smoothing using a Gaussian kernel of FWHM 5mm; grand-mean intensity normalisation of the entire 4D dataset by a single multiplicative factor; high-pass temporal filtering (Gaussian-weighted least-squares straight line fitting, with sigma=50.0s). Registration to high resolution structural (single subject GLM (general linear model)) and standard space (group-level GLM) images was carried out using FLIRT. Time-series analysis was carried out using FMRIB's Improved Linear Model (FILM) with local autocorrelation correction. To further correct for any potential movement confounds, motion regressors were estimated via MCFLIRT and scrubbed TRs were added as covariates of no interest to each individual design matrix. First-level fixed-effects model was then computed for each participant. Regressors were designed for each subject, created from the time course of the three experimental conditions (0, 1, and 2 back; between jittered fixation periods (4-8 seconds ISI)) and convolved with a canonical hemodynamic response function. For each subject, statistical contrast images of zero, one and two back > implicit baseline (fixation) were obtained.

To ensure that differences found in fMRI data were not attributed to head motion, we examined frame-wise displacement (FD) [3]. Average FDs were small (mean ± SD, pre-task: 0.08 ± 0.04 mm, post-task: 0.09 ± 0.06 mm), and a paired t-test revealed no significant difference between the two groups ($p = 0.12$).

Partitioning the Brain into Regions of Interest

In order to construct a dynamic functional connectivity graph, we have to first divide brain volume into anatomical brain areas. Using an anatomical atlas, we grouped voxels oriented within a coherent anatomical 3D space and we then averaged voxel-based BOLD time series to get a representative time series per ROI (for recent reviews, see [3–5]). Many atlases are available in the literature that divide the cortex into a restrict number of brain volumes [6-8]. A famous one is the Automated Anatomical Labeling (AAL) which is provided by the SPM toolbox [9]. In our study, we estimated the 90 representative mean BOLD time series by averaging voxel-based time series within brain areas defined by the AAL atlas.

Wavelet Decomposition

Brain function is highly frequency dependent while different cognitive (dys)functions are expressed in specific frequency bands. In previous studies, BOLD activity per ROI at both resting-state and task conditions has been decomposed via wavelets [10, 11]. Wavelet-based time series were robust to noise and sensitive to small changes in the activity [12]. The maximum-overlap discrete wavelet transform (MODWT) has been frequently used in exploring functional connectivity of fMRI [13–18]. Accordingly, we adopted MODWT to decompose each regional time series into wavelet scales corresponding to specific frequency bands [19]. Wavelet coefficients for the first four wavelet scales correspond to the frequency ranges 0.125∼0.25 Hz (Scale 1), 0.06∼0.125 Hz (Scale 2), 0.03∼0.06 Hz (Scale 3), and 0.015∼0.03 Hz (Scale 4) [20,21,22,24].

Connectivity Over Temporal Scale

Dynamic Connectivity Estimation

We constructed a dynamic functional connectivity graph for each n-back level and for each participant. As a connectivity estimator, we used wavelet-based coherence. Here, we have used wavelet-based coherence measure compared to the Pearson correlation coefficient for many reasons. The wavelet-based coherence is much more robust to many sources of artifacts like movement-related artifacts, enhances the signal to ratio of every BOLD time series simultaneously denoising the signal while its range of values is bounded over [0 1] and not in [-1 1] with both negative-positive correlations as with Pearson correlation coefficient.

We first concatenated regional mean time series per ROI over each n-back level [25]. We then constructed, a dynamic functional connectivity graph (DFCG) for each subject, based on the wavelet coherence between regional mean time series. We constructed a separate DFCG for each subject for each n-back level [3,25] for a total of 73 temporal FCG (87 TRs per condition, time-window=15 TRs, stepping moving criterion = 1TR, (87 - 15) + 1 = 73 temporal FCG) per subject. This number of slices can give a high temporal resolution of the dynamic functional connectivity strength.

Construction of Brain Networks

In many studies, the choice of an appropriate connectivity estimators was wavelet coherence [13,15,18,26,27]. In the dynamic brain network approach, we estimated the wavelet coherence between every pair of ROIs (a total of 4005 pair-wise associations) for every temporal segment oriented by the width of window of 15 slices with 1 slice overlap between consecutive temporal segments [28]. This approach yields a dynamic functional brain connectivity graph of size 73 x 90 x90 per frequency scale and per subject.

S3A-B illustrates how a DFCG has been estimated by adopting the sliding-window approach. In S5, one can understand how the DFCG has been constructed. We adjusted the selected time-window of 15 slices on the experimental BOLD activity and we estimated the quasi-static FCG. Then we moved the time-window by 1 slice and we re-estimated the FCG. The first time-window encapsulates 1-15 time slices, the second 2-16 slices and so on. Finally, we estimated the DFCG with three dimensions, the first referring to time windows and the last two to the 2D matrix representation of FCG that tabulates the temporal correlation of every pair of ROI BOLD time series.

Our goal was to construct multi-layer networks where the layers referred to the quasi-static functional brain networks estimated per temporal segment, here 73 in total per subject and frequency band. Till now, modularity in multi-layer networks has been estimated by assigning values of 1 as the weight of inter-slice connections. However, the inter-slice connections could fluctuate across experimental time (see S4). For that reason, we assigned the following weight to the link that connects every node i between two consecutive temporal segments (network layers):

$$\gamma^{i}_{[t,t+1]} = \frac{\sum_j w^{t}_{ij}\, w^{t+1}_{ij}}{\sqrt{s^{t}_{i} s^{t+1}_{i}}} \quad (1)$$

where w^{t}_{ij} are the weights derived from wavelet coherence between every pair {i,j} at time t while s^{t}_{i} is the total strength of node i over time snapshot t. γ^{i} takes values between 0 and 1. Higher values of γ^{i} can be obtained when the functional interactions of node persist across experimental time.

However, the aforementioned approach yields a fully-weighted dynamic functional connectivity graph while not all the pair-wise associations indicate the existence of functional associations [13]. Due the absence of a neurophysiological baseline of true functional associations, we need to generate surrogates that 'mimic' specific attributes of the original BOLD time series.

However, as pointed out in other network studies of fMRI data [13], not all elements $\mathbf{r_{i,j}}$ of the full correlation matrix necessarily indicate significant functional relationships. Many approaches have been suggested so far: the random approach, the Amplitude-Adjusted Fourier Transform (AAFT) surrogate and the iterative Amplitude-Adjusted Fourier Transform (iAAFT) surrogate. The random surrogate approach shuffles the samples of a time series reordering them across experimental time (see **S3.A**). However, this approach didn't preserve the variance, the mean and the autocorrelation function of the original time series. The second surrogate approach randomizes the phase of the time series in the Fourier space [28]

FT surrogate null models assumes that linear properties of the time series are defined via the squared amplitudes of the discrete Fourier transform (FT) expressed in the following equation

$$|S(u)|^2 = \left| \frac{1}{\sqrt{V}} \sum_{v=0}^{V-1} s_v e^{i2\pi uv/V} \right|^2 \quad (2)$$

where sv defines a sample of the time series with length equals to V. FT method is constructed by multiplying the Fourier transform of the original time series with uniformly randomized phases and then back transforming tin the time domain. This procedure is described in the following equation.

$$\bar{s}_v = \frac{1}{\sqrt{V}} \sum_{v=0}^{V-1} e^{ia_u} |S_u| e^{i2\pi kv/V} \quad (3)$$

where $a_u \in [0, 2\pi)$ are chosen independently and uniformly at random [30,[31]. A modification of this method is called amplitude-adjusted Fourier transform (AAFT) surrogate which retains the amplitude distribution of the original signal [32] (see S3.D). The fourth surrogate null model is called iteratively amplitude-adjusted Fourier transform (iAAFT) surrogate. iAAFT is an improved version of AAFT which iteratively, it fits the amplitudes and at each step improves the spectral phases and then reorders the derived time series at each step until convergence of both spectral density and amplitude distribution is reached. The algorithm terminates if complete convergence is succeeded.

In figure S3, we showed an example of how the surrogate null networks look like [33,34]. We averaged the functional brain networks across all layers from a single subject at each case. It seems that

iAAFT yields mean wavelet coherence values closest to the original and it was our choice for the surrogate analysis.

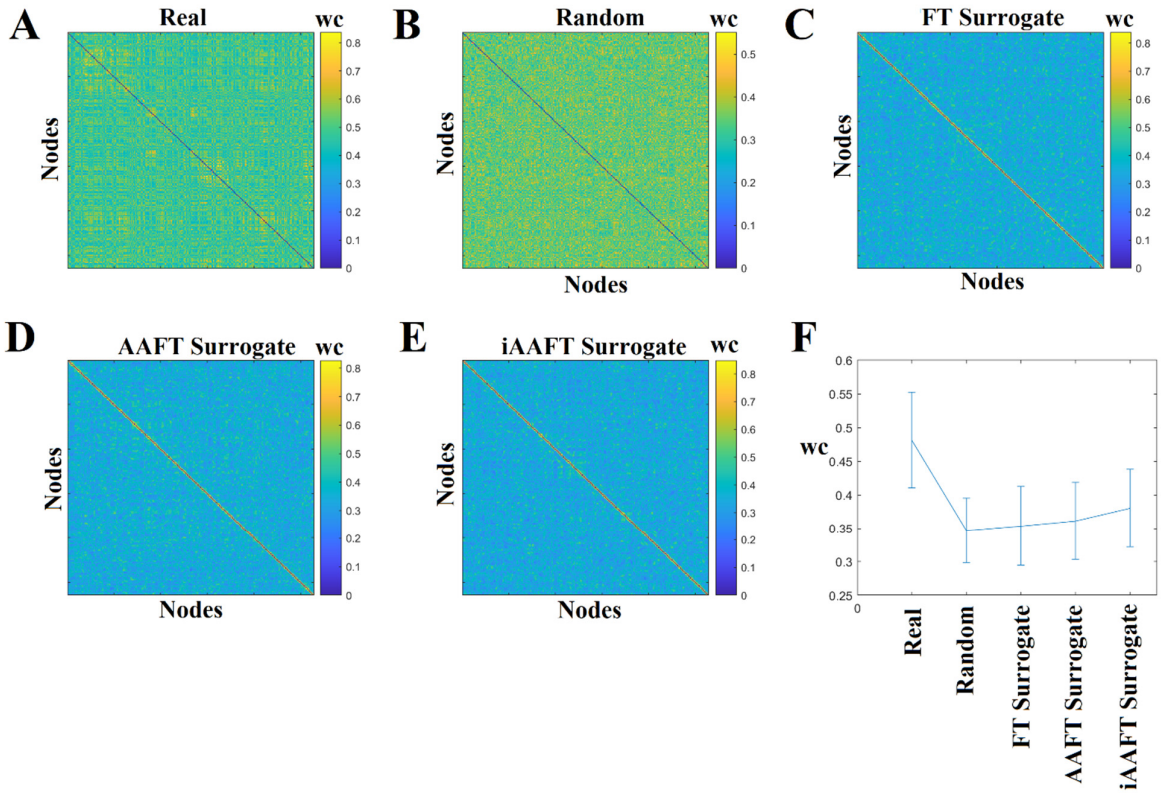

Figure S3. Available surrogate null models for time series and statistical filtering of functional wavelet coherence (WC).

(A) Example coherence matrix A^l averaged over layers from a brain network.

(B) Random surrogates, (C) FT surrogate, (D) AAFT surrogate null models , (E) iAAFT surrogate null models averaged over layers

(F) Wavelet Coherence (WC) of each matrix type averaged over subjects, n-back levels, and layers.

In the present study, we generated 1.000 surrogates per ROI time series leading to 1.000 values of coherence per pair of ROIs. Based on the distribution of the surrogate correlation values, we assigned a p-value per pair of ROIs and for each temporal segment [13,29]. We then tested the p-values $p_{i,j}$ for significance using a False Discovery Rate (FDR) of $p < 0.05$ to correct for multiple comparisons [30,31] independently for each quasi-static snapshot of the DFCG. All the connections that didn't pass the FDR correction approach were set to 0.

Additionally to the statistical filtering approach, we applied a data-driven topological filtering approach to further reveal the true network topology of each quasi-static FCG. Our method is called Orthogonal Minimal Spanning Tree (OMST) and was previously used in EEG, MEG and fMRI to improve the reliability of network metrics, brain fingerprinting, the discrimination of multiple-groups simultaneously and also the development of a novel chronnectomic brain-aged index [36-38].

Statistical and topological filtering of the dynamic functional connectivity brain graph is important to reveal the temporal communities via the multilayer network modularity. If the multi-layer is fully-weighted then the algorithm described in the next section will give a unique community and a low Q quality function. In many strong publications, the authors didn't report any statistical and topological filtering and it is an issue of how they found temporal modules.

Multilayer Network Modularity:

We attempted to characterize how brain areas are spatially and temporally connected across experimental time and in the n-back levels. Community detection algorithms is a powerful family of methods belonging to the large scientific research area of network neuroscience [32,33, 34]. A community is composed of a set of brain areas that are more connected between each other compared to the rest of the network. A popular approach to reveal communities is the optimization of the famous modularity Q function [39,40] expressed as:

$$Q = \sum_{ij} [A_{ij} - P_{ij}] \delta(g_i, g_j) \quad (4)$$

To reveal temporal communities that evolved over experimental time and to reveal the evolution of communities affiliations across brain systems, we constructed a multi-layer network. Every frame of the dynamic functional connectivity brain graph corresponds is a unique layer. The layers were linked here using equation 1 that quantifies the (in)stability of functional strength of every node between consecutive windows. Previous articles used a stable weight for the inter-slice connections equal to 1 [43].

A multilayer network was constructed for every subject in every n-back level. Then, we performed the famous Louvain greedy algorithm [44] optimizing the temporal extension of the famous modularity expressed in the following equation:

$$Q = \frac{1}{2\mu} \sum_{ijlr} \{(A_{ijl} - \gamma_l P_{ijl})\, \delta_{lr} + \delta_{ij}\omega_{jlr}\}\, \delta\,(g_{il}, g_{jr}) \quad (5)$$

where I refers to the layer (temporal segment), A_{ijl} is the functional brain network per layer (temporal segment), P_{ijl} are the components of every layer I matrix , γ_l is the structural resolution parameter of layer l, the quantity g_{il} gives the community assignment of node i in layer l, the g_{jr} is the community assignment of node j in layer r, the element ω_{jlr} refers to the connection strength from node j in layer r to node j in layer l, the total edge weight in the network is:

$$\mu = (1/2) \sum_{jr} k_{jr}$$

the strength (i.e., weighted degree) of node j in layer l is:

$$k_{jl} = k_{jl} + c_{jl}$$

the intralayer strength of node j in layer l is:

$$k_{jl} = \sum_{i} A_{ill}$$

and the interlayer strength of node j in layer l is:

$$c_{jl} = \sum_{r} \omega_{jlr}.$$

The whole procedure gives a community affiliation for every brain area at every temporal segment. However, the maximization of the temporal modularity quality function is an NP hard problem and the Louvain greedy algorithm is heuristic in the way of searching the optimal Q function (eq.5) [42]. We repeated 1000 times the Louvain greedy algorithm per pair of values for the two resolution parameters (γ_l ,ω_{jlr}) of the multilayer Q function that must be optimized (see next section).

Mucha's multilayer modularity algorithm was applied to the multi-layer DFCG illustrated in S4 [43]. We adopted Modularity Probability Method: MPM instead of default Maximum Modularity Method (MMM).

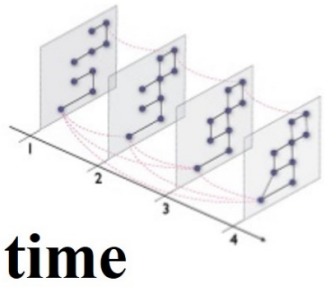

Figure S4. A multi-layer temporal network with inter-slice connections [43].

Figure S5 illustrates the steps of creating a DFCG from BOLD time series using wavelet coherence (A-B), the estimation of dynamic modules (C) and finally the calculation of the diagnostic called flexibility index (D).

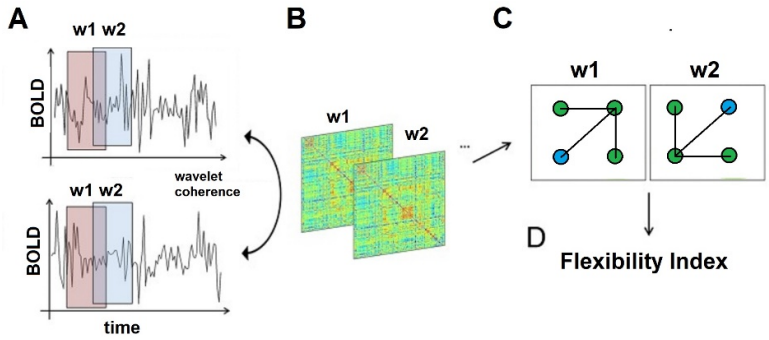

Figure S5. Construction of a dynamic functional connectivity brain network and the estimation of the Flexibility (F) index.

(*A*) An example of a pair Blood oxygen level-dependent (BOLD) signals from two brain regions defined in the AAL. (*B*) For every temporal segment w1,w2,… a functional connectivity graph is constructed of size NxN where N denotes the 90 ROIs (*C*) The maximization of the temporal extension of modularity algorithm by Mucha et al. yields spatio-temporal communities linking both space and time dimensions [43]. (*D*) Then, we estimated nodal Flexibility, *F*, as the number of times its community affiliation changes over temporal segments (see S13).

Statistical Framework

A first drawback of previous attempts to reveal temporal communities over a multi-layer network was their analysis over fully-weighted dynamic brain networks. Mucha's multilayer modularity algorithm has two basic parameters that must be optimized: the γl which is the structural resolution

parameter of layer l and the element ωjlr gives the temporal resolution parameter. In our scenario, we adopted proper surrogate null models tailored to temporal networks. Surrogate null models for static brain networks have been already proposed and used [27,44].

Here, we constructed three independent temporal surrogate null models tailored to temporal brain networks: (1) the first one will test the topology of the network, (2) the second will test the network structure dependent on nodal identity and (3) the third will test the temporal ordering of the layers in the multi-layer formulation.

Figure S6.A illustrates the quasi-static FCG for a single time window without inter-slice connections while **S6.B** illustrates the dynamic network with inter-slice connections.

In the connectional null model (1), we shuffled the connections of the network in every layer by preserving the degree of every node (S6.C). In the constructing nodal null model (2), we changed the inter-layer connection of every node with itself in every layer by randomly chosen nodes in layers. We followed this type of model in all the layers with the exception of the last layer. The weight inter-slice γ^i is re-estimated after the connectional null model. In the temporal structure model, we randomly permuted the order of the layers (temporal segments) (**S6.C**).

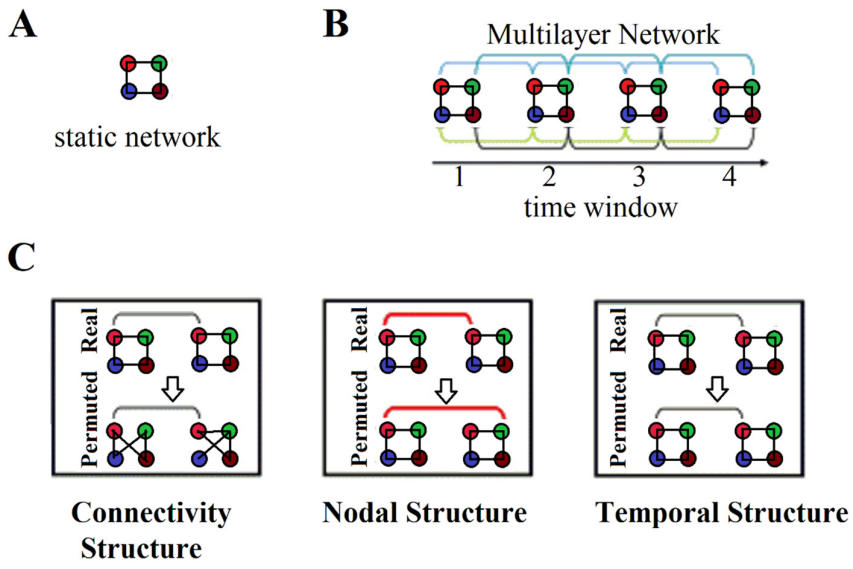

Figure S6. Temporal dynamics of modular architecture.

(A) A toy network example consisted of four nodes and four connections

(B) A multilayer network framework consisted of four temporal segments/layers linked by inter-slice connections in the adjacent time windows over homologue nodes (colored curves).

(C) Statistical framework of the three null modesl

The connectional null model , the nodal null model, and the temporal null model in which intra-network links, inter-network links, and layers or temporal segments, respectively, in the real network are randomized, respectively, in the permuted network.

Our main goal of using null models for the multi-layer graphs was to optimize the parameters of the Q function and namely the, γ_l which is the structural resolution parameter of layer l and the element ω_{jlr} gives the temporal resolution parameter. Searching from a range of values 0 – 3 with step 0.1 in both parameters, we detected the optimal pair of values independently for n-back level and for each subject separately. The main goal was to find the optimal pair of parameter values that minimize the p-value of the original Q over Qsurr estimated from the surrogate null models. Combining the optimization of the pair of parameter that influences the Q quality index and the heuristic Louvain greedy algorithm, we run Louvain algorithm 1000 times per pair of values over the searching space.

It is the very first time that a study attempted to optimize the the, γ_l which is the structural resolution parameter of layer l and the element ω_{jlr} gives the temporal resolution parameter by adopting surrogate network null models. Previous studies used default parameters equal to 1 [41].

Statistical Testing

For every subject, frequency scale and n-back level, we detected the pair of parameters (γ_l , ω_{jlr}) that minimizes the p-value of Q quality function when we compared the mean Q value over 1000 runs over the original multi-layer network with the surrogate mean Q values reproduced over 1000 surrogate null models using simultaneously the three types of temporal surrogate null models. Specifically, for every pair of values for the two parameters (γ_l , ω_{jlr}), we created 1000 surrogate multi-layer networks and for every surrogate temporal null model, we run 1000 times the Louvain greedy algorithm as we did for the original multi-layer network. Then, we first averaged the Q values over the 1000 runs of Louvain algorithm giving a total number of 1000 surrogate Q values per pair of values of the two parameters. Comparing the original Q value with the 1000 surrogate Q values, we assigned a p-value of Q over the 2d searching space the pair of parameters (γ_l , ω_{jlr}). Then, we found the minimum p-value to get the optimal pair of values for the (γ_l , ω_{jlr}).

Flexibility index was estimated per node across the 1000 runs of Louvain algorithm for the optimal set of (γ_l , ω_{jlr}). For every run, we tabulated in a $FR_{i,j}$ matrix as binary elements whether self-node ii changes its community affiliation between two consecutive time windows at every transition j. Averaging all runs of temporal modularity optimization, we ‘ve got the average flexibility index matrix

FR whose elements in the main diagonal $FR_{i,j}$ report the probability that a brain area change community affiliation over time.

Mean Q value and mean number of modules were estimated over 1000 runs of Louvain algorithm for the optimal values of the set (γ_1 , ω_{jlr}).

We found an optimal set of parameters { γ_1 , ω_{jlr} } per frequency scale and group (table S3). Following a Wilcoxon Signed Rank-Sum test, no significant group differences were detected for both parameters across the four frequency scales ($p< 0.05$).

Table S3. Mean and Standard deviations of { γ_1 , ω_{jlr}} per frequency scale and group.

Frequency Scales	**1** { γ_1 , ω_{jlr} }	**2** { γ_1 , ω_{jlr} }	**3** { γ_1 , ω_{jlr} }	**4** { γ_1 , ω_{jlr} }
Low SCH-PRS	γ=1.07±0.02 ω=2.53±0.02	γ=1.07±0.02 ω=2.52±0.02	γ=1.06±0.02 ω=2.51±0.02	γ=1.05±0.02 ω=2.51±0.02
High SCH-PRS	γ=1.06±0.02 ω=2.51±0.05	γ=1.06±0.02 ω=2.52±0.02	γ=1.06±0.02 ω=2.52±0.02	γ=1.06±0.02 ω=2.52±0.02

Temporal Dynamics of Brain Architecture

In the present study, we have attempted to determine whether changes in the dynamic modular architecture of functional connectivity is shaped by polygenic risk score for schizophrenia. Modular architecture may vary with cognitive workload and it could be altered due to polygenic risk score for schizophrenia.

The number of module or the modularity index Q encapsulates the changes of modular architecture during experimental paradigm. Changes of the composition of modules is quantified by the nodal flexibility index F_i which expresses the probability of a node to change community affiliation over time. FI can be averaged over nodes constituted well know brain networks such as fronto-parietal network, default mode network etc.

Unique Characteristics of our Approach

Our dynamic functional brain connectivity graph analysis is unique in the literature in multiple ways:

(1) We statistically and topologically filtering our fully-weighted brain networks across layers (temporal segments)

(2) We estimated inter-slice connection with γ^i (eq.1) instead of using a default parameter of 1 as in [41,48,49]

(3) We optimized the pair of parameters (γ_1 , ω_{jlr}) instead of using a default parameter of 1 as in [41,48,49] via surrogate temporal null models

(4) We run 1000 times the Louvain greedy algorithm to get stable findings due to its heuristic nature

(5) The optimization of the pair of parameters (γ_1 , ω_{jlr}) has been realized independently per subject,n-back level and frequency scale over the minimization of the p-value related to the Q quality index of the original multilayer network compared to 1000 surrogate null multi-layer models

(6) The whole analysis has been realized independently per subject, n-back level and frequency scale

Statistics and Software

We implemented all computational and simple statistical operations using the software package MATLAB (2007a, The MathWorks Inc., Natick,MA). We performed network calculations using a combination of in-house software and the open implementation of the multi-layer community detection code [43]. fMRI data were preprocessed using the FMRIB Software Library (FSL) analysis package.

Supplementary Results

Task Performance

As expected for an n-back task, we found a main effect of load condition with lower proportion of correct responses for higher load conditions ($p < 0.001$, Wilcoxon Rank Sum Test). We found no interaction between load and group ($p > 0.671$, Wilcoxon Rank Sum Test) and no significant group difference ($p > 0.563$, Wilcoxon Rank Sum Test). Group means are shown in figure S7.

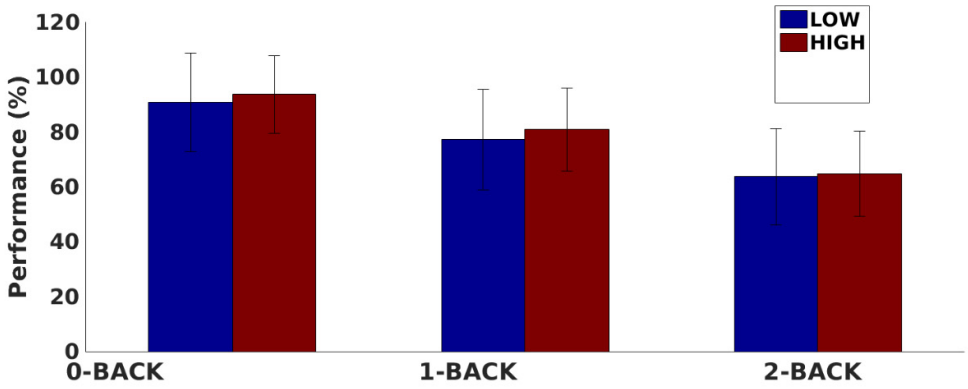

Figure S7. Task performance (% correct answers) of both groups across the n-back levels (Wilcoxon Rank Sum Test , $p > 0.563$).

Number of Temporal Modules and Modularity Q_{ml}

S8 illustrates the group-averaged number of temporal modules across n-back levels and frequency ranges. The group with low SCZ-PRS demonstrates significantly higher Q_{ml} and higher number of temporal modules across n-back levels and frequency ranges. All the Q_{ml} were significant compared to the adopted null model ($p < 0.001$).

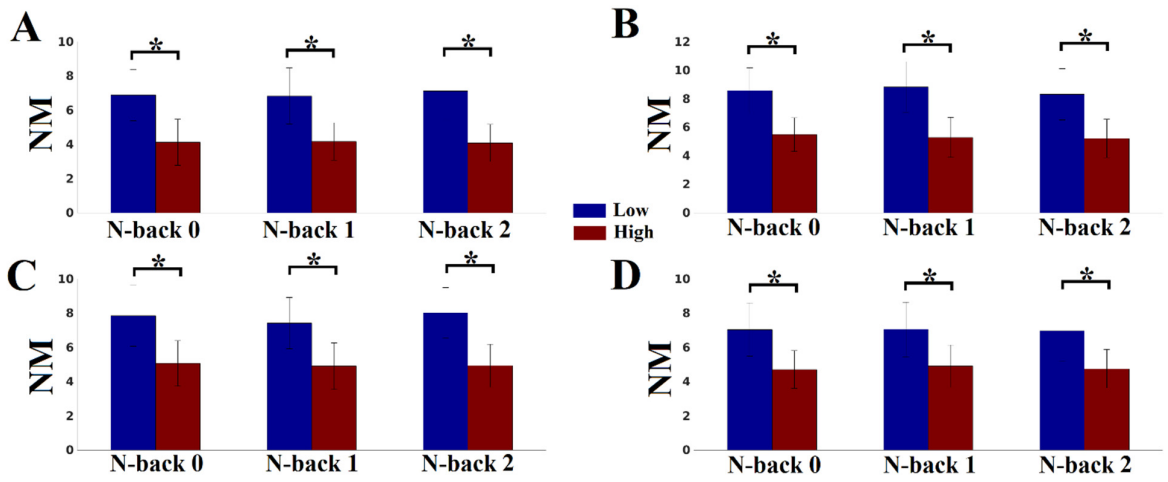

Figure S8. Group-average of the number of modules NM across n-back levels and frequency scales (A-D)

A.0.125~0.25 Hz (Scale 1)

B. 0.06~0.125 Hz (Scale 2)

C.0.03~0.06 Hz (Scale 3), and

D.0.015~0.03 Hz (Scale 4)

(* Wilcoxon Rank Sum Test , p< 0.01)

Topologies of Group-Averaged Flexibility Index across Frequency Sub-bands

S9-S12 illustrate the group-averaged FI per ROI for each n-back level and specifically for frequency range 1, 2 and 4 like in Fig. 3 in the main text. S13 demonstrates the FI across frequency bands and working memory levels integrated within 5 well-known brain networks.

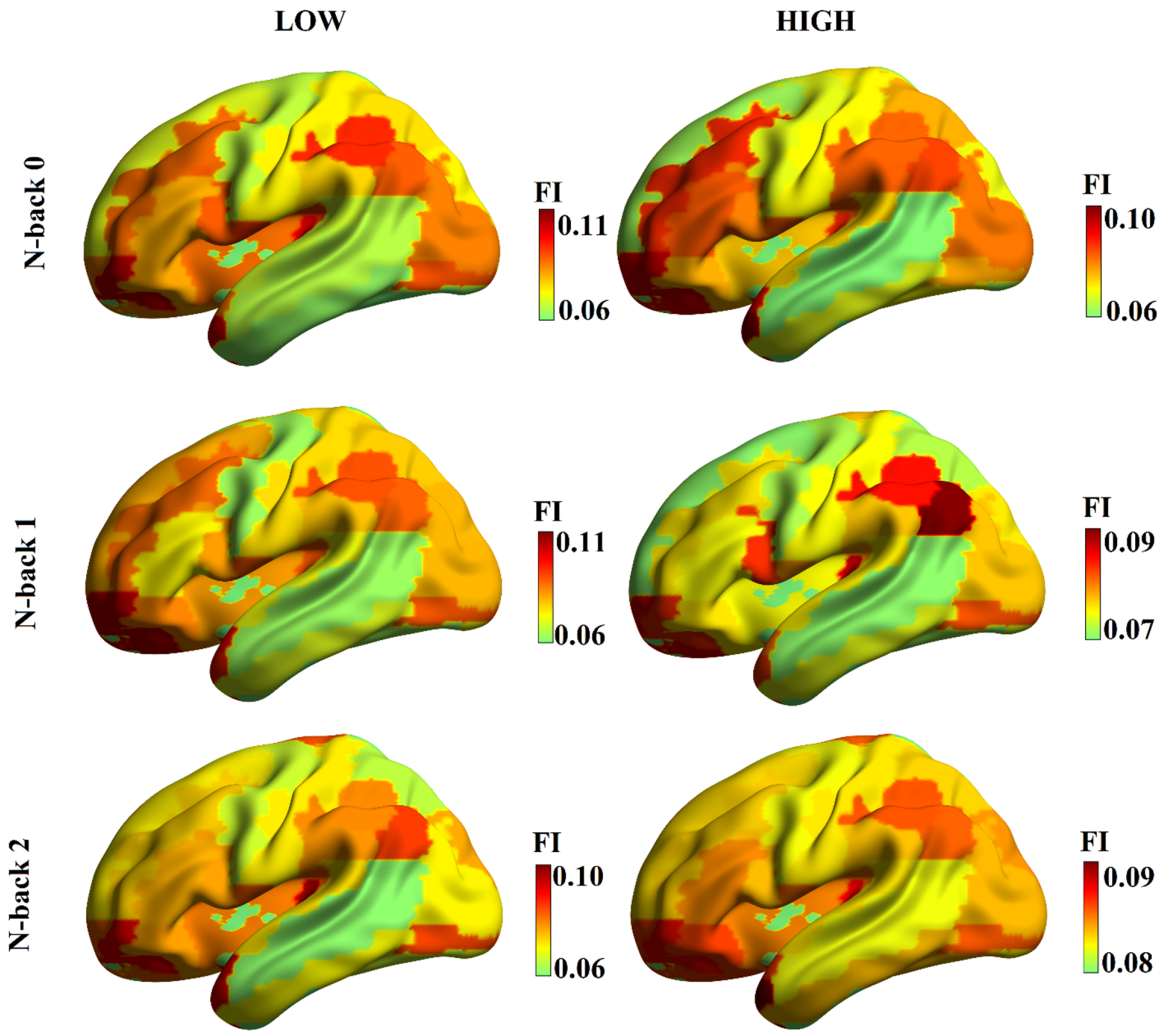

Figure S9. Group averaged FI per ROI for each n-back level at frequency scale 1 (0.125~0.25 Hz).

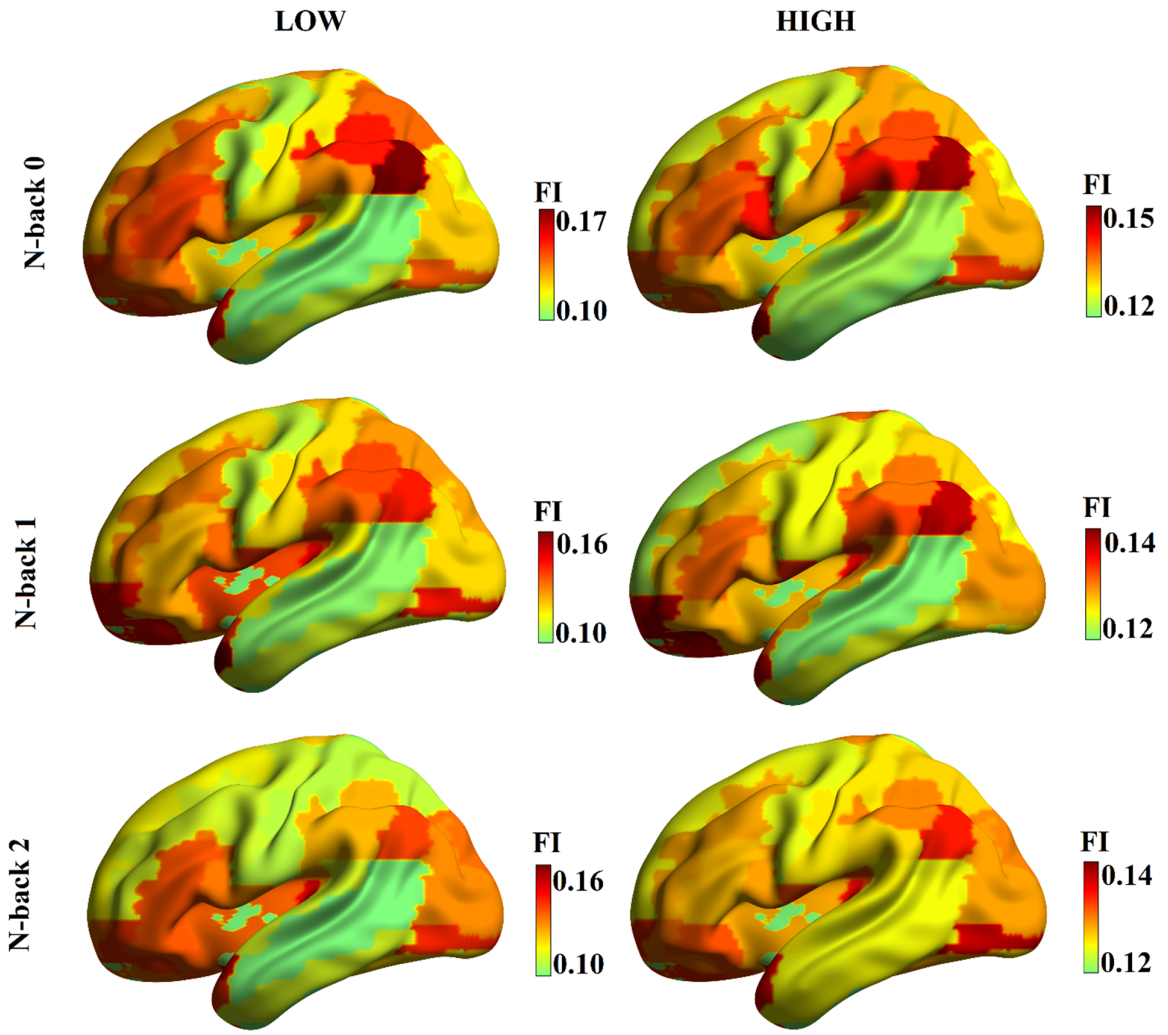

Figure S10. Group averaged FI per ROI for each n-back level at frequency scale 2 (0.06~0.125 Hz).

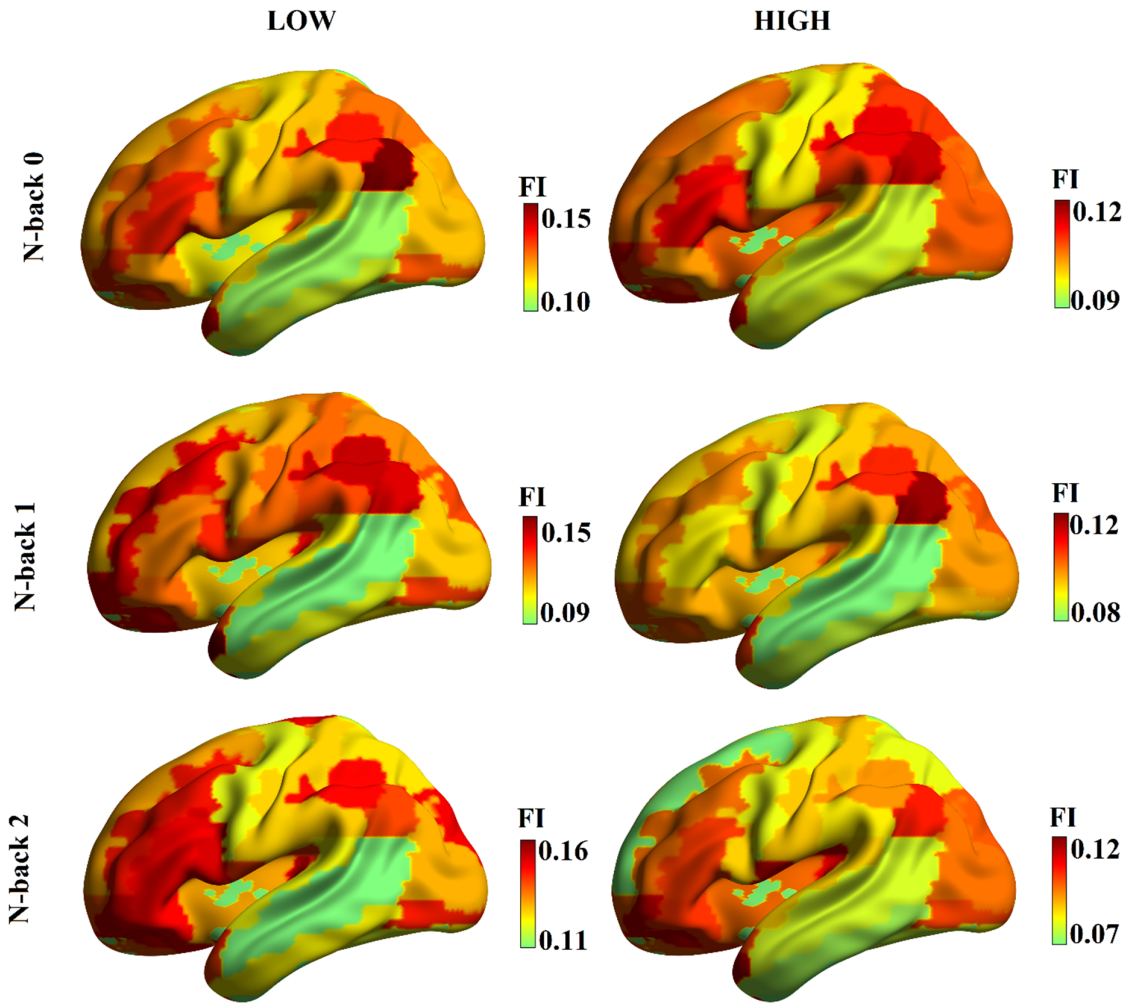

Figure S11. Group averaged FI per ROI for each n-back level at frequency scale 3 (0.03~0.06 Hz).

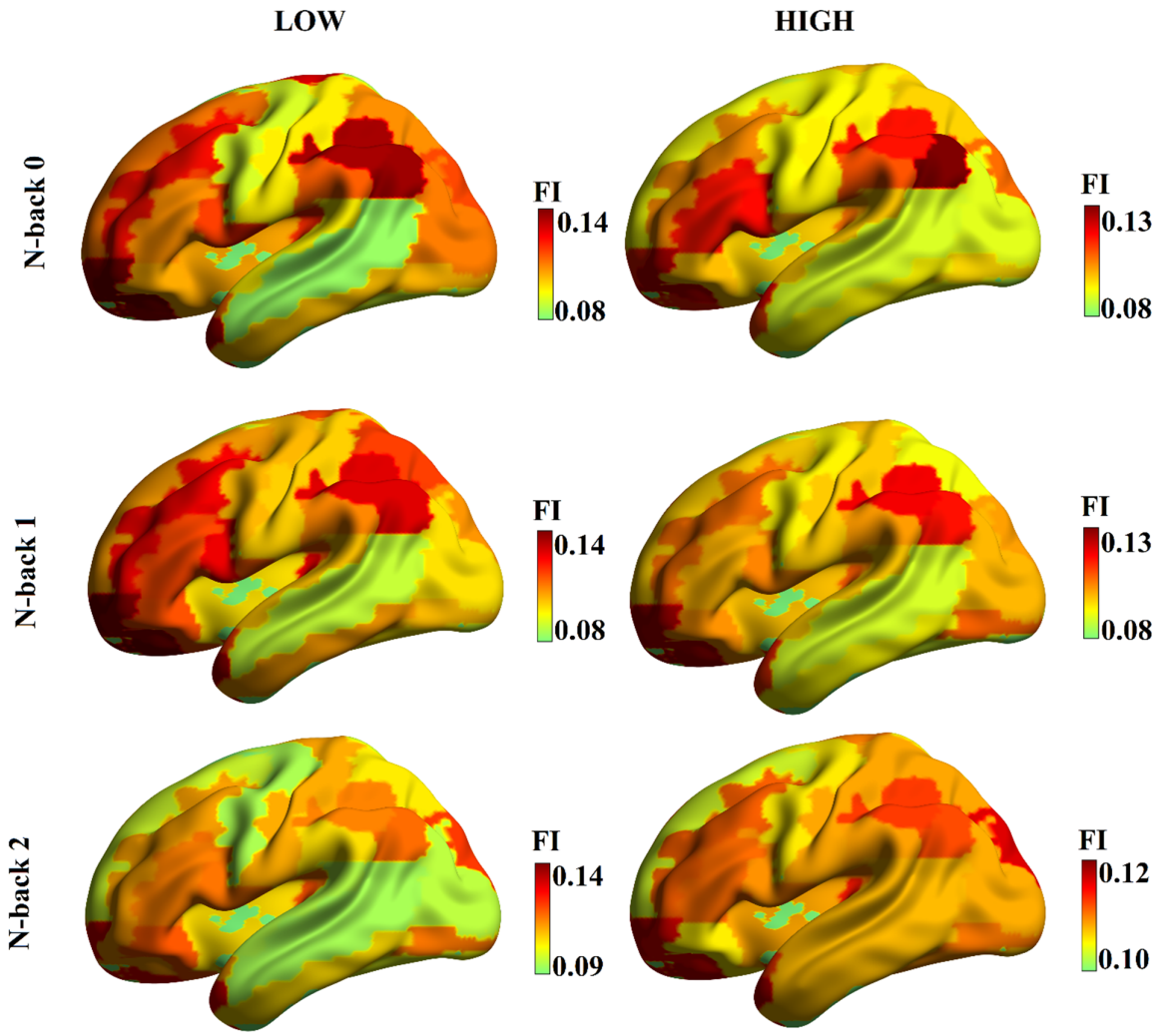

Figure S12. Group averaged FI per ROI for each n-back level at frequency scale 4 (0.015~0.03Hz).

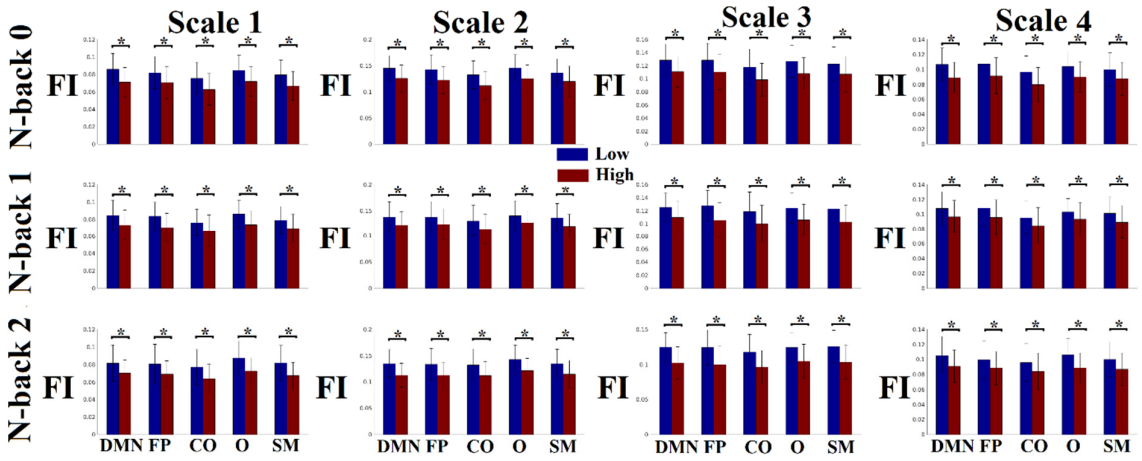

Figure S13. Group-averaged Flexibility Index (FI) across n-back level and frequency scales for the five brain networks.

FI was significantly higher for the group with low SCZ-PRS compared to the group with the high SCZ-PRS across frequency scales and n-back levels

(* Wilcoxon Rank Sum Test, $p < 0.05$, Bonferroni Corrected $p' < p/12$ where 12 denotes the 3 working memory levels multiplied by the 4 frequency scales

DMN: Default Mode Network, FP: Fronto-Patieral, CO: Cingulo-Opercular, O: Occipital and SM: SensoriMotor

0.125~0.25 Hz (Scale 1), 0.06~0.125 Hz (Scale 2), 0.03~0.06 Hz (Scale 3), and 0.015~0.03 Hz (Scale 4))

Effect of the Time Window Length

In the construction of dynamic functional connectivity graph (dFCG), the selection of time window length T could play a pivotal role. The time window length should not be too short and not too long in order to capture the alterations of functional interactions during a cognitive task [56]. In the main text, we reported results for time windows of 15 data points in length. This gives 41 time windows in each n-back level. Shortening or lengthening the time window T will have a big impact to the variation of functional connectivity strength over experimental time [16]. To probe with the effect of the appropriate selection of time window length, we varied T from T = 17 to T = 21 with steps equal to 2 TR (see S14). Group differences over global FI are still preserved for the three additional time windows T.

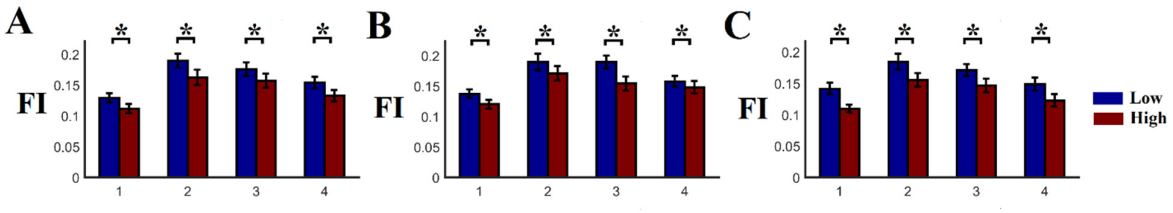

Figure S14: Effect of the time window length T on the Global FI in this study:

Group-averaged global FI and standard deviations across participants. Global FI findings for: A) T=17, B) T=19 and C) T=21 TRs

Numbers 1-4 refer to the following frequency scales:

1. 0.125~0.25 Hz (Scale 1),
2. 0.06~0.125 Hz (Scale 2),
3. 0.03~0.06 Hz (Scale 3), and
4. 0.015~0.03 Hz (Scale 4)

Multi-linear Regression Analysis of FI and Behavioural Performance

Employing the 360 nodal FI values (4 frequency scales x 90 ROIs) as independent variables, we applied a multi-linear regression analysis to extract the nodal FI that can predict behavioral performance. We applied this modelling approach independently for each n-back level and frequency band with the main aim of revealing the most informative frequency range and brain network. To diminish the effect of multi-collinearity and also take into account the non-linear relationships of the FI predictors, we adopted a stepwise regression model as implemented in MATLAB with the *stepwiselm* function. To validate our approach, we adopted a leave-one out approach measuring the mean error across individuals.

For comparison purposes, we followed the same procedure using the BOLD activity (as per the GLM approach) to further enhance the dynamic functional brain connectivity to better describe task performance.

In order to link the notion of nodal FI with behavioral performance on the n-back task, we followed a multi-linear regression analysis. We decided to use the 360 nodal FI from the 90 ROIs and from the four frequency scales in order to reveal the contribution of each frequency scale to the performance. S13 illustrates the beta coefficients of the 360 nodal FI independently for the two groups and n-back level. For a better understanding on the topology of the brain networks involved in this prediction, we integrated the 90 ROI into five well-known brain networks: **DMN - FP - O - CO – SM** for Default

Mode Network, Fronto-Parietal, Occipital, Cingulo-Opercular and SensoriMotor. The time series of the beta coefficients was derived by averaging the results across the 10-folds.

We adopted a 10-fold cross-validation strategy in order to avoid overfitting the model and also to increase the generalization of the findings. Subsequently, mean squared errors were estimated between the original performance and the one predicted across the 10-folds. Also, mean squared errors and R^2 were estimated across the 10-folds. The results are demonstrated in the following Table.

We performed a multi-linear regression analysis to establish how well behavioral performance at every n-back level could be predicted using the nodal FI from each frequency sub-band and the brain BOLD activity as an independent set of variables. The whole analysis was repeated independently for group, frequency scale, n-back level and GLM/FI in both whole-brain and Fronto-Parietal Network (FPN). We followed a 10-fold cross-validation scheme where at every run the multi-linear model trained on nine folds, and then tested on the remaining fold. R^2 and p-values were averaged across the 10-fold cross-validation scheme.

R^2 of the multi-linear model of global FI and behavioral performance across the 10-folds was high for every n-back level, reaching 0.77 on average in both groups (minimum 0.66) (Table S4.a).The FI of the FP network accounted for almost half of the prediction of behavioral performance (Table S4.b) with higher FI corresponding to better performance. The difference between the prediction from whole-brain FI and FPN FI was significant (Wilcoxon Rank-Sum test of the R^2 obtained for n-back level, frequency scale and group: $p < 0.034x10^{-6}$).

The average R^2 of the multi-linear model of the whole brain BOLD activity and behavioral performance across the 10-folds reached 0.35 on average in both groups and were thus in the similar range as the predictions from the FI of the FPN (Table S4.c). R^2 related to BOLD activity of the FPN was slightly lower than the prediction from whole brain BOLD activity (Table S4.d). This difference was also significant (Wilcoxon Rank-Sum test of the R^2 obtained for n-back level, frequency scale and group: $p < 0.051x10^{-4}$).

Finally, R^2 in n-back levels, in frequency scales and in both groups were significantly higher for FI compared to GLM-derived BOLD activity estimates ($p < 0.067x10^{-5}$). This analysis demonstrates that the FI of dynamic functional brain activity explained behavioral performance better than the task-based BOLD activity in both groups and across n-back levels and frequency scales.

Table S4. Group-averaged R^2 derived from multi-linear modelling of FP FI (Table S4.a) , whole-brain FI (Table S4.b), whole-brain BOLD activity (Table S4.c) and FP BOLD activity (Table S4.d) with behavioural performance. We followed a multi-linear modelling independently for each subject, n-back level and FrSc. The results were averaged across subjects within each group (rows) and n-back levels including the four FrSc (columns). P-values refer to the statistical level of the modelling which further support their interpretation. (FrSc:Frequency Scale)
(Frequency ranges 0.125∼0.25 Hz (Scale 1), 0.06∼0.125 Hz (Scale 2), 0.03∼0.06 Hz (Scale 3), and 0.015∼0.03 Hz (Scale 4))

Table S4.a Multi-linear modelling of **whole brain FI (nodal FI) and behavioural performance** averaged across the 10-folds for the three n-back levels and independently for the groups. R^2/p-values estimates have been averaged across the 10-folds.

	n-back 0: FrSc^1/ FrSc^2/ FrSc^3/ FrSc^4	**n-back 1: FrSc^1/ FrSc^2/ FrSc^3/ FrSc^4**	**n-back 2: FrSc^1/ FrSc^2/ FrSc^3/ FrSc^4**
Low SCH-PRS	**0.69 ±0.06 pval=0.00051±0.00041 / 0.73 ±0.05 pval=0.00243 ± 0.00034/ 0.74 ±0.06 pval=0.00415 ±0.00122/ 0.77 ±0.05 pval=0.00066±0.000033**	**0.68 ±0.05 pval=0.000109 ±0.000084/ 0.74 ±0.06 pval=0.000282 ±0.000082/ 0.75 ±0.07 pval=0.000344 ±0.000101/ 0.76 ±0.07 pval=0.000543 ±0.000112**	**0.67 ±0.06 pval=0.000641 ±0.000013/ 0.71 ±0.08 pval=0.000433 ±0.000128/ 0.74 ±0.06 pval=0.000566±0.000148/ 0.75 ±0.08 pval=0.000864±0.000213**
High SCH-PRS	**0.68 ±0.07 pval=0.00514±0.00021 / 0.72 ±0.08 pval=0.00377 ±0.00145/ 0.74 ±0.08 pval=0.00511 ±0.00205/ 0.76 ±0.07 pval=0.00436±0.00172**	**0.67 ±0.08 pval=0.00431±0.00197 / 0.72 ±0.07 pval=0.00502±0.00122 / 0.73 ±0.08 pval=0.00429± 0.00101/ 0.74 ±0.06 pval=0.00521±0.00231**	**0.66 ±0.05 pval=0.00432±0.00128/ 0.70 ±0.05 pval=0.000421±0.000315 / 0.72 ±0.07 pval=0.000341± 0.000255/ 0.73 ±0.08 pval=0.000161±0.006**

Table S4.b. Multi-linear modelling of **nodal FI from the FP network and behavioural performance** averaged across the 10-folds for the three n-back levels and independently for the groups. R^2/p-values estimates have been averaged across the 10-folds.

	n-back 0: $FrSc^1$/ $FrSc^2$/ $FrSc^3$/ $FrSc^4$	**n-back 1: $FrSc^1$/ $FrSc^2$/ $FrSc^3$/ $FrSc^4$**	**n-back 2: $FrSc^1$/ $FrSc^2$/ $FrSc^3$/ $FrSc^4$**
Low SCH-PRS	**0.31 ± 0.07 pval=0.0043 $\pm$0.0001 / 0.35 ± 0.06 pval=0.0051 $\pm$ 0.0021 / 0.34 ± 0.07 pval=0.0056 $\pm$ 0.0018 / 0.35 ± 0.07 pval=0.0078 $\pm$ 0.0023**	**0.30 ± 0.06 pval=0.0044 $\pm$0.0021 / 0.34 ± 0.06 pval=0.0069 $\pm$ 0.0021 / 0.35 ± 0.07 pval=0.0041 $\pm$0.0012 / 0.36 ± 0.05 pval=0.0053 $\pm$0.0027**	**0.31 ± 0.05 pval=0.0057 $\pm$0.0031 / 0.32 ± 0.05 pval=0.0056 $\pm$ 0.0021 / 0.33 ± 0.06 pval=0.0057 $\pm$ 0.0013 / 0.34 ± 0.07 pval=0.0057 $\pm$ 0.0021**
High SCH-PRS	**0.30 ± 0.06 pval=0.0062 $\pm$ 0.0022 / 0.33 ± 0.05 pval=0.0071 $\pm$ 0.0021 / 0.32 ± 0.06 pval=0.0033 $\pm$ 0.0019 / 0.33 ± 0.05 pval=0.0078 $\pm$ 0.0023**	**0.31 ± 0.08 pval=0.0056 $\pm$0.0031 / 0.33 ± 0.07 pval=0.0061 $\pm$ 0.0023 / 0.34 ± 0.07 pval=0.0056 $\pm$ 0.0021 / 0.35 ± 0.08 pval=0.0048 $\pm$ 0.0012**	**0.31 ± 0.06 pval=0.0061 $\pm$ 0.0023 / 0.32 ± 0.07 pval=0.0061 $\pm$ 0.0026 / 0.33 ± 0.08 pval=0.0063 $\pm$ 0.0031 / 0.34 ± 0.07 pval=0.0071 $\pm$ 0.0034**

Table S4.c Multi-linear modelling of BOLD activation levels from **the whole brain and behavioural performance** averaged across subjects for the three n-back levels and independently for the groups. R^2/p-values estimates have been averaged across the 10-folds.

	n-back 0: $FrSc^1$/ $FrSc^2$/ $FrSc^3$/ $FrSc^4$	**n-back 1: $FrSc^1$/ $FrSc^2$/ $FrSc^3$/ $FrSc^4$**	**n-back 2: $FrSc^1$/ $FrSc^2$/ $FrSc^3$/ $FrSc^4$**
Low SCH-PRS	**0.28 ± 0.05 pval=0.0047$\pm$$0.0012$/ 0.31 ± 0.06 pval=0.0052$\pm$$0.0021$/ 0.33 ± 0.04 pval=0.0056$\pm$$0.0026$/ 0.35 ± 0.06 pval=0.0062$\pm$$0.0022$**	**0.27 ± 0.06 pval=0.0052 $\pm$0.0024 / 0.31 ± 0.07 pval=0.0056$\pm$$0.0031$/ 0.33 ± 0.06 pval=0.0048$\pm$$0.0021$/ 0.35 ± 0.07 pval=0.0058$\pm$$0.0023$**	**0.28 ± 0.07 pval=0.0068 $\pm$ 0.031 / 0.30 ± 0.06 pval=0.0047$\pm$$0.0034$ / 0.32 ± 0.05 pval=0.0064$\pm$$0.0042$ / 0.35 ± 0.06 pval=0.0041$\pm$$0.016$**

High SCH-PRS	**0.27 ±0.06 pval=0.0063 ±0.0031 / 0.30 ±0.07 pval=0.0062±0.0023/ 0.32 ±0.07 pval=0.0063±0.0022/ 0.34 ±0.08 pval=0.0046±0.0017**	**0.26 ±0.06 pval=0.00710.0023 / 0.29 ±0.05 pval=0.0056±0.0031/ 0.32 ±0.07 pval=0.0043±0.0023/ 0.34 ±0.05 pval=0.0065±0.0021**	**0.26 ±0.06 pval=0.0052±0.031/ 0.28 ±0.07 pval=0.0031±0.0008/ 0.30 ±0.06 pval=0.0044±0.0012/ 0.32 ±0.05 pval=0.0051±0.0022**

Table S4.d. Multi-linear modelling of BOLD activation levels from **the FP network and behavioural performance** averaged across the 10-folds for the three n-back levels and independently for the groups. R^2/p-values estimates have been averaged across the 10-folds.

	n-back 0: FrSc^1/ FrSc^2/ FrSc^3/ FrSc^4	**n-back 1: FrSc^1/ FrSc^2/ FrSc^3/ FrSc^4**	**n-back 2: FrSc^1/ FrSc^2/ FrSc^3/ FrSc^4**
Low SCH-PRS	**0.20 ±0.06 pval=0.0043 ± 0.0031 / 0.22 ±0.05 pval=0.0054± 0.0022/ 0.23 ±0.04 pval=0.0061±0.0012/ 0.24 ±0.04 pval=0.0047±0.0012**	**0.21 ±0.05 pval=0.0036±0.0012/ 0.22 ±0.03 pval=0.00034±0.0028/ 0.24 ±0.06 pval=0.00063±0.0062/ 0.25 ±0.04 pval=0.0036±0.0007/**	**0.22 ±0.05 pval=0.00032 ± 0.0041/ 0.23 ±0.06 pval=0.0026±0.002/ 0.22 ±0.04 pval=0.0036±0.003/ 0.24 ±0.03 pval=0.00031±0.0045/**
High SCH-PRS	**0.20 ±0.06 pval=0.0021±0.0003/ 0.23 ±0.06 pval=0.0041±0.0017/ 0.21 ±0.06 pval=0.0056±0.0023/ 0.24 ±0.06 pval=0.0042±0.0021**	**0.22 ±0.04 pval=0.0012 ± 0.0005/ 0.24 ±0.05 pval=0.0038±0.006/ 0.25 ±0.06 pval=0.0018±0.0003/ 0.23 ±0.03 pval=0.00045±0.0043**	**0.22 ±0.04 pval=0.00052 ± 0.0043/ 0.23 ±0.05 pval=0.00047±0.0056/ 0.25 ±0.06 pval=0.00051±0.0071/ 0.24 ±0.05 pval=0.00039±0.0054**

A Note on Computational Time

The investigations that we report in the present work involved about 10,000 CPU-days, and our study was therefore made possible by the use of two computing clusters available at the CUBRIC Neuroimaging Center. Cluster 1 was composed of 42 Dell SC1425s (dual single-core Xeon 2.8GHz, 4GB memory), 5 Dell PE1950s (dual quad-core Xeon E5335 2.0GHz, 8GB memory) and 128 worker licenses (cluster has 124 compute cores).

Supplemental References

1. Lancaster TM,Dimitriadis SI, et al.,Structural and Functional Neuroimaging of Polygenic Risk for Schizophrenia: A Recall-by-Genotype-Based Approach. Schizophr Bull. 2018 Mar 28. doi: 10.1093/schbul/sby037. [Epub ahead of print]
2. Smith SM, M. Jenkinson, M. W. Woolrich, C. F. Beckmann, T. E. J. Behrens, H. Johansen-Berg, P. R. Bannister, M. De Luca, I. Drobnjak, D. E. Flitney, R. Niazy, J. Saunders, J. Vickers, Y. Zhang, N. De Stefano, J. M. Brady, and P. M. Matthews, "Advances in functional and structural MR image analysis and implementation as FSL," Neuroimage, vol. 23, no. S1, pp. 208–219, 2004.
3. D. S. Bassett and E. T. Bullmore, "Small-world brain networks," Neuroscientist, vol. 12, pp. 512–523,2006.
4. D. S. Bassett and E. T. Bullmore, "Human brain networks in health and disease," Curr Opin Neurol, vol. 22, no. 4, pp. 340–347, 2009.
5. E. Bullmore and O. Sporns, "Complex brain networks: Graph theoretical analysis of structural and functional systems," Nat Rev Neurosci, vol. 10, no. 3, pp. 186–198, 2009.
6. J. Wang, L. Wang, Y. Zang, H. Yang, H. Tang, Q. Gong, Z. Chen, C. Zhu, and Y. He, "Parcellation-dependent small-world brain functional networks: A resting-state fMRI study," Hum Brain Mapp, vol. 30, no. 5, pp. 1511–1523, 2009.
7. A. Zalesky, A. Fornito, I. H. Harding, L. Cocchi, M. Yucel, C. Pantelis, and E. T. Bullmore, "Whole-brain anatomical networks: Does the choice of nodes matter?," Neuroimage, vol. 50, no. 3, pp. 970–983, 2010.
8. D. S. Bassett, J. A. Brown, V. Deshpande, J. M. Carlson, and S. T. Grafton, "Conserved and variable architecture of human white matter connectivity," Neuroimage, vol. 54, no. 2, pp. 1262–79, 2011.
9. N. Tzourio-Mazoyer; B. Landeau; D. Papathanassiou; F. Crivello; O. Etard; N. Delcroix; Bernard Mazoyer & M. Joliot (January 2002). "Automated Anatomical Labeling of activations in SPM using a Macroscopic Anatomical Parcellation of the MNI MRI single-subject brain". NeuroImage. 15 (1): 273–289.
10. E. Bullmore, J. Fadili, M. Breakspear, R. Salvador, J. Suckling, and M. Brammer, "Wavelets and statistical analysis of functional magnetic resonance images of the human brain," Stat Methods Med Res, vol. 12, no. 5, pp. 375–399, 2003
11. E. Bullmore, J. Fadili, V. Maxim, L. Sendur, B. Whitcher, J. Suckling, M. Brammer, and M. Breakspear, "Wavelets and functional magnetic resonance imaging of the human brain," Neuroimage, vol. 23, no. 1, pp. S234–S249, 2004.
12. M. J. Brammer, "Multidimensional wavelet analysis of functional magnetic resonance images," Hum Brain Mapp, vol. 6, no. 5-6, pp. 378–382, 1998.
13. S. Achard, R. Salvador, B. Whitcher, J. Suckling, and E. Bullmore, "A resilient, low-frequency, small-world human brain functional network with highly connected association cortical hubs," J Neurosci, vol. 26, no. 1, pp. 63–72, 2006.
14. S. Achard, D. S. Bassett, A. Meyer-Lindenberg, and E. Bullmore, "Fractal connectivity of long-memory networks," Phys Rev E, vol. 77, no. 3, p. 036104, 2008
15. D. S. Bassett, A. Meyer-Lindenberg, S. Achard, T. Duke, and E. Bullmore, "Adaptive reconfigu- ration of fractal small-world human brain functional networks," Proc Natl Acad Sci USA, vol. 103, pp. 19518–19523, 2006.

16. S. Achard and E. Bullmore, “Efficiency and cost of economical brain functional networks,” PLoS Comput Biol, vol. 3, p. e17, 2007.

17. D. S. Bassett, A. Meyer-Lindenberg, D. R. Weinberger, R. Coppola, and E. Bullmore, “Cogni- tive fitness of cost-efficient brain functional networks,” Proc Natl Acad Sci USA, vol. 106, no. 28, pp. 11747–11752, 2009.

18. M. E. Lynall, D. S. Bassett, R. Kerwin, P. McKenna, U. Muller, and E. T. Bullmore, “Functional connectivity and brain networks in schizophrenia,” J Neurosci, vol. 30, no. 28, pp. 9477–87, 2010.

19. D. B. Percival and A. T. Walden, Wavelet Methods for Time Series Analysis. Cambridge University

Press, 2000.

20. F. T. Sun, L. M. Miller, and M. D’Esposito, “Measuring interregional functional connectivity using coherence and partial coherence analyses of fMRI data,” Neuroimage, vol. 21, no. 2, pp. 647–658,2004.

21. A. Barnes, E. T. Bullmore, and J. Suckling, “Endogenous human brain dynamics recover slowly following cognitive effort,” PLoS One, vol. 4, no. 8, p. e6626, 2009.

22. M. J. Lowe, B. J. Mock, and J. A. Sorenson, “Functional connectivity in single and multislice echoplanar imaging using resting state fluctuations,” Neuroimage, vol. 7, pp. 119–132, 1998.

23. D. Cordes, V. M. Haughton, K. Arfanakis, G. J. Wendt, P. A. Turski, C. H. Moritz, M. A. Qugley, and M. E. Meyerand, “Mapping functionally related regions of brain with functional connectivity MR imaging,” Am J Neuroradiol, vol. 21, pp. 1636–1644, 2000.

24. D. Cordes, V. M. Haughton, K. Arfanakis, J. D. Carew, P. A. Turski, C. H. Moritz, M. A. Quigley, and M. E. Meyerand, “Frequencies contributing to functional connectivity in the cerebral cortex in “resting-state” data,” Am J Neuroradiol, vol. 22, no. 7, pp. 1326–1333, 2001.

25. D. A. Fair, B. L. Schlaggar, A. L. Cohen, F. M. Miezin, N. U. Dosenbach, K. K. Wenger, M. D. Fox, A. Z. Snyder, M. E. Raichle, and S. E. Petersen, “A method for using blocked and event-related fMRI data to study ‘resting state’ functional connectivity,” Neuroimage, vol. 35, no. 1, pp. 396–405,

26. 2007.

27. D. Meunier, S. Achard, A. Morcom, and E. Bullmore, “Age-related changes in modular organization of human brain functional networks,” Neuroimage, vol. 44, no. 3, pp. 715–723, 2008.

28. Van De Ville D(2015) On spurious and real fluctuations of dynamic functional connectivity during rest. Neuroimage 104:430–436

29. D. Meunier, R. Lambiotte, A. Fornito, K. D. Ersche, and E. T. Bullmore, “Hierarchical modularity in human brain functional networks,” Front Neuroinformatics, vol. 3, p. 37, 2009.

30. D. Prichard and J. Theiler, Phys. Rev. Lett. 73, 951 (1994).

31. H. Nakatani, I. Khalilov, P. Gong, and C. van Leeuwen, Phys. Lett. A 319, 167 (2003).

32. A. Zalesky, A. Fornito, and E. Bullmore, Neuroimage 60, 2096 (2012).

33. J. Theiler, S. Eubank, A. Longtin, B. Galdrikian, and J. D. Farmer, Physica D 58, 77 (1992).

34. C. Räth, M. Gliozzi, I. E. Papadakis, and W. Brinkmann, Phys. Rev. Lett. 109, 144101 (2012).

35. G. Rossmanith, H. Modest, C. Räth, A. J. Banday, K. M. Gorski, and G. Morfill, Phys. Rev. D 86, 083005 (2012)

36. Dimitriadis, S.et al. 2017a. Topological filtering of dynamic functional brain networks unfolds informative chronnectomics: a novel data-driven thresholding scheme based on Orthogonal Minimal Spanning Trees (OMSTs). Frontiers in Neuroinformatics 11, article number: 28

37. Dimitriadis SI, Salis CI (2017b). Mining Time-Resolved Functional Brain Graphs to an EEG-Based Chronnectomic Brain Aged Index (CBAI). Front. Hum. Neurosci., 07 September 2017 | https://doi.org/10.3389/fnhum.2017.00423

38. Dimitriadis, S.et al. 2017c. Data-driven topological filtering based on orthogonal minimal spanning trees: application to multi-group MEG resting-state connectivity. Brain Connectivity (10.1089/brain.2017.0512)

39. M. A. Porter, J.-P. Onnela, and P. J. Mucha, "Communities in networks," Not Amer Math Soc, vol. 56, no. 9, pp. 1082–1097, 1164–1166, 2009

40. S. Fortunato, "Community detection in graphs," Phys Rep, vol. 486, no. 3–5, pp. 75–174, 2010.

41. Bassett DS, et al.(2011) Dynamic reconfiguration of human brain networks during learning. Proc Natl Acad Sci USA 108(18):7641–764

42. Jutla I, Jeub L, Mucha P (2011) A generalized Louvain method for community detection implemented in MATLAB (computer program).

43. P. J. Mucha, T. Richardson, K. Macon, M. A. Porter, and J.-P. Onnela, "Community structure in time-dependent, multiscale, and multiplex networks," Science, vol. 328, no. 5980, pp. 876–878, 2010.

44. D. S. Bassett, D. L. Greenfield, A. Meyer-Lindenberg, D. R. Weinberger, S. Moore, and E. Bullmore, "Efficient physical embedding of topologically complex information processing networks in brains and computer circuits," PLoS Comput Biol, vol. 6, no. 4, p. e1000748, 2010.

45. Stuss DT(2006) Frontal lobes and attention: Processes and networks, fractionation and integration.J Int Neuropsychol Soc 12(2):261–271

46. V. D. Blondel, J. L. Guillaume, R. Lambiotte, and E. Lefebvre, "Fast unfolding of community hierarchies in large networks," J Stat Mech, p. P10008, 2008.

47. Jenkinson, M., Beckmann, C.F., Behrens, T.E., Woolrich, M.W., Smith, S.M. (2012) Fsl. Neuroimage, 62:782-790.

48. U. Braun, *et al.*Dynamic reconfiguration of frontal brain networks during executive cognition in humans.Proc. Natl. Acad. Sci. U.S.A., 112 (2015), pp. 11678-11683

49. U. Braun, *et al.*Dynamic brain network reconfiguration as a potential schizophrenia genetic risk mechanism modulated by NMDA receptor function.Proc. Natl. Acad. Sci. U. S. A., 113 (2016), pp. 12568-12573